Nano-optical single-photon response mapping of waveguide integrated molybdenum silicide (MoSi) superconducting nanowires

Jian Li,[1,3,4] **Robert A. Kirkwood,**[1] **Luke J. Baker,**[1] **David Bosworth,**[2] **Kleanthis Erotokritou,**[1] **Archan Banerjee,**[1] **Robert M. Heath,**[1] **Chandra M. Natarajan,**[1] **Zoe H. Barber,**[2] **Marc Sorel,**[1] **and Robert H. Hadfield**[1,5]

[1]*School of Engineering, University of Glasgow, Glasgow, G12 8LT, United Kingdom*
[2]*Department of Materials Science & Metallurgy, University of Cambridge, Cambridge CB3 0FS, United Kingdom*
[3]*Current address: Interdisciplinary Center of Quantum Information, College of Science, National University of Defense Technology, Changsha 410073, China*
[4]*Jian.Li@glasgow.ac.uk*
[5]*Robert.Hadfield@glasgow.ac.uk*

Abstract: We present low temperature nano-optical characterization of a silicon-on-insulator (SOI) waveguide integrated SNSPD. The SNSPD is fabricated from an amorphous $Mo_{83}Si_{17}$ thin film chosen to give excellent substrate conformity. At 350 mK, the SNSPD exhibits a uniform photoresponse under perpendicular illumination, corresponding to a maximum system detection efficiency of approximately 5% at 1550 nm wavelength. Under these conditions 10 Hz dark count rate and 51 ps full width at half maximum (FWHM) timing jitter is observed.

OCIS codes: (230.5160) Photodetectors; (220.0220) Optical design and fabrication; (230.3120) Integrated optics devices; (270.5570) Quantum detectors.

References and links

1. H. Takesue, S. W. Nam, Q. Zhang, R. H. Hadfield, T. Honjo, K. Tamaki, and Y. Yamamoto, "Quantum key distribution over a 40-dB channel loss using superconducting single-photon detectors," Nat. Photonics **1**, 343–348 (2007).
2. D. Stucki, N. Walenta, F. Vannel, R. T. Thew, N. Gisin, H. Zbinden, S. Gray, C. R. Towery, and S. Ten, "High rate, long-distance quantum key distribution over 250km of ultra low loss fibres," New J. Phys. **11**, 075003 (2009).
3. B. Korzh, C. C. W. Lim, R. Houlmann, N. Gisin, M. J. Li, D. Nolan, B. Sanguinetti, R. Thew, and H. Zbinden, "Provably secure and practical quantum key distribution over 307km of optical fibre," Nat. Photonics **9**, 163–168 (2015).
4. E. Knill, R. Laflamme, and G. J. Milburn, "A scheme for efficient quantum computation with linear optics," Nature **409**, 46–52 (2001).
5. P. Kok, W. J. Munro, K. Nemoto, T. C. Ralph, J. P. Dowling, and G. J. Milburn, "Linear optical quantum computing with photonic qubits," Rev. Mod. Phys. **79**, 135 (2007).
6. J. L. O'Brien, "Optical quantum computing," Science **318**, 1567–1570 (2007).
7. G. N. Gol'tsman, O. Okunev, G. Chulkova, A. Lipatov, A. Semenov, K. Smirnov, B. Voronov, A. Dzardanov, C. Williams, and R. Sobolewski, "Picosecond superconducting single-photon optical detector," Appl. Phys. Lett. **79**, 705 (2001).
8. S. Miki, M. Fujiwara, M. Sasaki, B. Baek, A. J. Miller, R. H. Hadfield, S. W. Nam, and Z. Wang, "Large sensitive-area NbN nanowire superconducting single-photon detectors fabricated on single-crystal MgO substrates," Appl. Phys. Lett. **92**, 061116 (2008).

#260601 Received 7 Mar 2016; revised 13 May 2016; accepted 18 May 2016; published 14 Jun 2016

9. C. M. Natarajan, M. G. Tanner, and R. H. Hadfield, "Superconducting nanowire single-photon detectors: physics and applications," Supercond. Sci. Technol. **25**, 063001 (2012).
10. M. G. Tanner, C. M. Natarajan, V. K. Pottapenjara, J. A. O'Connor, R. J. Warburton, R. H. Hadfield, B. Baek, S. Nam, S. N. Dorenbos, E. B. Ureña, T. Zijlstra, T. M. Klapwijk, and V. Zwiller, "Enhanced telecom wavelength single-photon detection with NbTiN superconducting nanowires on oxidized silicon," Appl. Phys. Lett. **96**, 221109 (2010).
11. B. Baek, A. E. Lita, V. Verma, and S. W. Nam, "Superconducting a-W_xSi_{1-x} nanowire single-photon detector with saturated internal quantum efficiency from visible to 1850 nm," Appl. Phys. Lett. **98**, 251105 (2011).
12. F. Marsili, V. B. Verma, J. A. Stern, S. Harrington, A. E. Lita, T. Gerrits, I. Vayshenker, B. Baek, M. D. Shaw, R. P. Mirin, and S. W. Nam, "Detecting single infrared photons with 93% system efficiency," Nat. Photonics **7**, 210–214 (2013).
13. V. B. Verma, A. E. Lita, M. R. Vissers, F. Marsili, D. P. Pappas, R. P. Mirin, and S. W. Nam, "Superconducting nanowire single photon detectors fabricated from an amorphous $Mo_{0.75}Ge_{0.25}$ thin film," Appl. Phys. Lett. **105**, 022602 (2014).
14. Y. P. Korneeva, M. Y. Mikhailov, Y. P. Pershin, N. N. Manova, A. V. Divochiy, Y. B. Vakhtomin, A. A. Korneev, K. V. Smirnov, A. G. Sivakov, A. Y. Devizenko, and G. N. Goltsman, "Superconducting single-photon detector made of MoSi film," Supercond. Sci. Technol. **27**, 095012 (2014).
15. A. A. Korneev, Y. P. Korneeva, M. Y. Mikhailov, Y. P. Pershin, A. V. Semenov, D. Y. Vodolazov, A. V. Divochiy, Y. B. Vakhtomin, K. V. Smirnov, A. G. Sivakov, A. Y. Devizenko, and G. N. Goltsman, "Characterization of MoSi superconducting single-photon detectors in the magnetic field," IEEE Trans. Appl. Supercond. **25**, 2200504 (2015).
16. V. B. Verma, B. Korzh, F. Bussières, R. D. Horansky, S. D. Dyer, A. E. Lita, I. Vayshenker, F. Marsili, M. D. Shaw, H. Zbinden, R. P. Mirin, and S. W. Nam, "High-efficiency superconducting nanowire single-photon detectors fabricated from MoSi thin-films," Opt. Express **23**, 33792–33801 (2015).
17. H. Takesue, S. D. Dyer, M. J. Stevens, V. Verma, R. P. Mirin, and S. W. Nam, "Quantum teleportation over 100km of fiber using highly efficient superconducting nanowire single-photon detectors," Optica **2**, 832–835 (2015).
18. X. Hu, C. W. Holzwarth, D. Masciarelli, E. A. Dauler, and K. K. Berggren, "Efficiently coupling light to superconducting nanowire single-photon detectors," IEEE Trans. Appl. Supercond. **19**, 336 (2009).
19. A. Politi, M. J. Cryan, J. G. Rarity, S. Yu, and J. L. O'Brien, "Silica-on-silicon waveguide quantum circuits," Science **320**, 646–649 (2008).
20. J. P. Sprengers, A. Gaggero, D. Sahin, S. Jahanmirinejad, G. Frucci, F. Mattioli, R. Leoni, J. Beetz, M. Lermer, M. Kamp, S. Höfling, R. Sanjines, and A. Fiore, "Waveguide superconducting single-photon detectors for integrated quantum photonic circuits," Appl. Phys. Lett. **99**, 181110 (2011).
21. G. Reithmaier, S. Lichtmannecker, T. Reichert, P. Hasch, K. Mueller, M. Bichler, R. Gross, and J. Finley, "On-chip time resolved detection of quantum dot emission using integrated superconducting single photon detectors," Sci. Rep. **3**, 1901 (2013).
22. W. H. P. Pernice, C. Schuck, O. Minaeva, M. Li, G. N. Goltzman, A. V. Sergienko, and H. X. Tang, "High-speed and high-efficiency travelling wave single-photon detectors embedded in nanophotonic circuits," Nat. Commun. **3**, 1325 (2012).
23. M. G. Tanner, L. S. E. Alvarez, W. Jiang, R. J. Warburton, Z. H. Barber, and R. H. Hadfield, "A superconducting nanowire single photon detector on lithium niobate," Nanotechnology **23**, 505201 (2012).
24. C. Schuck, W. H. P. Pernice, and H. X. Tang, "Waveguide integrated low noise NbTiN nanowire single-photon detectors with milli-Hz dark count rate," Sci. Rep. **3**, 1893 (2013).
25. F. Najafi, J. Mower, N. C. Harris, F. Bellei, A. Dane, C. Lee, X. Hu, P. Kharel, F. marsili, S. Assefa, K. K. Berggren, and D. Englund, "On-chip detection of non-classical light by scalable integration of single-photon detectors," Nat. Commun. **6**, 5873 (2015).
26. D. Bosworth, S.-L. Sahonta, R. H. Hadfield, and Z. H. Barber, "Amorphous molybdenum silicon superconducting thin films," AIP Adv. **5**, 087106 (2015).
27. J. R. Clem and K. K. Berggren, "Geometry-dependent critical currents in superconducting nanocircuits," Phys. Rev. B **84**, 174510 (2011).
28. C. E. de Nobriga, G. D. Hobbs, W. J. Wadsworth, J. C. Knight, D. V. Skryabin, A. Samarelli, M. Sorel, and R. M. D. L. Rue, "Supermode dispersion and waveguide-to-slot mode transition in arrays of silicon-on-insulator waveguides," Opt. Lett. **35**, 3925 (2010).
29. R. S. Bhatia, S. T. Chase, S. F. Edgington, J. Glenn, W. C. Jones, A. E. Lange, B. Maffei, A. K. Mainzer, P. D. Mauskopf, B. J. Philhour, and B. K. Rownd, "A three-stage helium sorption refrigerator for cooling of infrared detectors to 280 mK," Cryogenics **40**, 685–691 (2000).
30. R. M. Heath, M. G. Tanner, A. Casaburi, M. G. Webster, L. S. E. Alvarez, W. Jiang, Z. H. Barber, R. J. Warburton, and R. H. Hadfield, "Nano-optical observation of cascade switching in a parallel superconducting nanowire single photon detector," Appl. Phys. Lett. **104**, 063503 (2014).
31. J. A. O'Connor, M. G. Tanner, C. M. Natarajan, G. S. Buller, R. J. Warburton, S. Miki, Z. Wang, S. W. Nam, and R. H. Hadfield, "Spatial dependence of output pulse delay in a niobium nitride nanowire superconducting single-photon detector," Appl. Phys. Lett. **98**, 201116 (2011).

#260601 Received 7 Mar 2016; revised 13 May 2016; accepted 18 May 2016; published 14 Jun 2016

32. A. J. Annunziata, O. Quaranta, D. F. Santavicca, A. Casaburi, L. Frunzio, M. Ejrnaes, M. J. Rooks, R. Cristiano, S. Pagano, A. Frydman, and D. E. Prober, "Reset dynamics and latching in niobium superconducting nanowire single-photon detectors," J. Appl. Phys. **108**, 084507 (2010).
33. M. K. Akhlaghi, E. Schelew, and J. F. Young, "Waveguide integrated superconducting single-photon detectors implemented as near-perfect absorbers of coherent radiation," Nat. Commun. **6**, 8233 (2014).
34. M. Varnava, D. E. Browne, and T. Rudolph, "How good must single photon sources and detectors be for efficient linear optical quantum computation?" Phys. Rev. Lett. **100**, 060502 (2008).

1. Introduction

Telecom-band near-infrared light with wavelengths of approximately 1.5 μm offers low loss over long distances in optical fibers and low loss in integrated silicon photonic circuits. This wavelength band is therefore an excellent choice for emerging quantum information processing applications such as quantum key distribution (QKD) [1–3] and optical quantum computing (OQC) [4–6]. High performance single-photon detectors at this wavelength range underpin all of these applications. QKD applications can use stand-alone fiber-coupled single photon detector packages, however, scalable OQC requires that single-photon sources and detectors as well as other nanophotonic elements are integrated into a monolithic chip.

Superconducting nanowire single photon detectors (SNSPDs) can offer high detection efficiency and ultrafast detection rate of single photons across a large spectral range. Since the first niobium nitride (NbN) SNSPD [7] demonstrated in 2001, there has been a rapid progress in SNSPD technology. However, the polycrystalline nature of NbN restricts choice of substrate materials and device fabrication yield [8,9]. Large superconducting gap energies of NbN and niobium titanium nitride (NbTiN) [10] also limit the intrinsic detection efficiency of long wavelength (lower energy) photons. Thus in recent years much attention has been given to amorphous superconductors with smaller gap energies, such as tungsten silicide (WSi) [11,12], molybdenum germanium (MoGe) [13] and molybdenum silicide (MoSi) [14,15]. By integrating into optical stack cavities, WSi meander SNSPDs have demonstrated 93% system detection efficiency (SDE) for telecom wavelength single photons [12], which coupled with intrinsically low dark counts, sets a new benchmark in telecom wavelength single photon detection. Very recently, MoSi SNSPDs have been integrated into optical cavities and fiber-coupled, demonstrating high efficiency coupled with low timing jitter [16]. Quantum teleportation over optical fiber has reached more than 100 km with the help of four MoSi meander SNSPDs [17].

Apart from the stand-alone meander SNSPDs, another kind of design called traveling wave or waveguide integrated SNSPD [18] allows easy monolithic integration of SNSPDs into nanophotonic circuits. This design has been experimentally realized by fabricating NbN or NbTiN SNSPDs on top of optical waveguides [19] in various material systems, including gallium arsenide (GaAs) [20,21], silicon-on-insulator (SOI) [22], lithium niobate (LN) [23] and silicon nitride (SiN) [24]. The main advantage of traveling wave SNSPDs is their long interaction lengths with photons traveling underneath, which improves photon absorption probability. Traveling wave SNSPDs also have advantages in device fabrication yield and uniformity. Since the length of nanowires in traveling wave SNSPDs is normally less than 10% of that in meander SNSPDs, it is easier to pattern a uniform nanowire with shorter length, and thus less likely to have constrictions and defects in traveling wave SNSPDs. A high yield process of fabricating NbN SNSPDs on SiN membranes [25] has been developed very recently for scalable integration of multiple SNSPDs in one monolithic nanophotonic circuit.

In this work, we combine the advantages of amorphous MoSi and the traveling wave SNSPD design. This paper presents characterization of a hairpin-shape MoSi SNSPD fabricated on top of a single-mode SOI waveguide. To characterize the uniformity and performance of our SOI waveguide integrated MoSi SNSPD, we have constructed a cryogenic nano-optical test setup with a base temperature of 350 mK.

#260601 Received 7 Mar 2016; revised 13 May 2016; accepted 18 May 2016; published 14 Jun 2016

2. Materials and methods

Amorphous MoSi films were grown by DC magnetron sputtering at University of Cambridge. The sputtering recipe was optimized by varying the composition of Mo_xSi_{1-x} and cooling the substrate during film growth [26]. A critical temperature $T_c = 7.6$ K was reported for 100 nm thick amorphous $Mo_{83}Si_{17}$ on top of silicon [26]. Film used for fabricating the SNSPD presented in this paper was 10 nm thick $Mo_{83}Si_{17}$ capped with 5 nm thick silicon deposited on SOI [220 nm silicon on 2 μm silicon dioxide, see Fig. 1(a)] substrate. The SNSPD nanowire width was 140 nm, the gap between two nanowires was 90 nm wide, and the headstock [27] length is 450 nm, as shown in Fig. 1(b). The devices were then patterned and fabricated in James Watt Nanofabrication Centre at University of Glasgow.

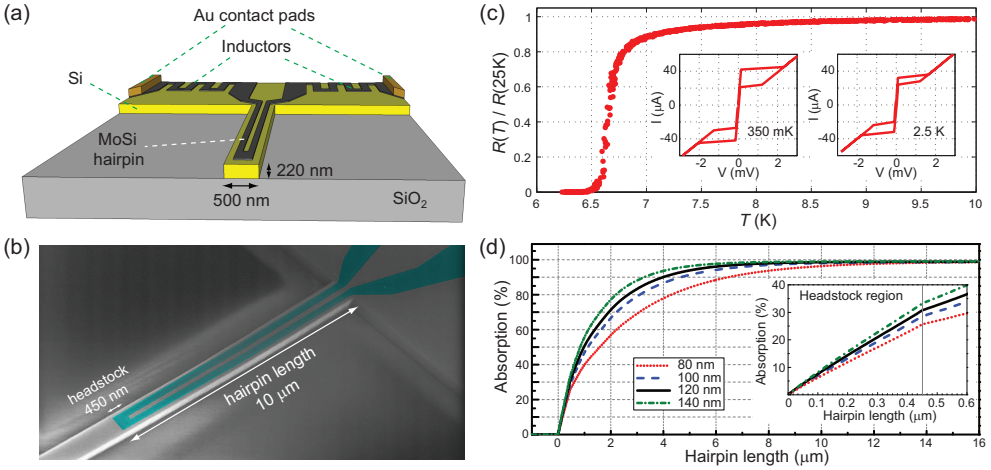

Fig. 1. (a) Sample cross-section sketch, showing the SOI single-mode (500 nm $\times$ 220 nm) waveguide, the MoSi SNSPD on top of it and the Au contact pads. (b) Scanning electron microscope (SEM) image of the MoSi hairpin SNSPD (false colored) and the SOI waveguide. (c) Normalized device resistance versus temperature. The insets are current-voltage characteristics of the device at 350 mK (left) and 2.5 K (right), respectively (two-wire measurement). The critical current: $I_c = 41$ μA at 350 mK, and $I_c = 32$ μA at 2.5 K. (d) Simulated absorption efficiencies of 1550 nm wavelength light versus MoSi hairpin length for four different nanowire widths (80 nm, 100 nm, 120 nm and 140 nm). The gap width between two nanowires is fixed at 90 nm. Refractive index $n = 5.2502$ and extinction coefficient $k = 4.7736$ are used for the simulations. The insert is an enlarged view of the absorption efficiencies in the headstock region.

Three electron-beam lithography (EBL) steps were used during the fabrication process. All EBL steps used 110 nm thick ZEP 520A positive tone electron-beam resist, and were carried out by a Vistec VB6 UHR EHF EBL tool at 100 keV. The first EBL step patterned alignment markers and bonding contact pads. After development, 85 nm thick Au (with 10 nm Ti adhesion layer) markers and contact pads were deposited by ultrahigh vacuum electron-gun evaporation and lift-off. The hairpin, the inductors and the measurement electrodes were patterned in the second EBL step. Then the patterns were transferred into the MoSi film by reactive ion etching (RIE) with CF_4. The waveguide pattern was defined in the last EBL step and transfered to the top Si layer of the SOI substrate by a fluorine-based inductively coupled plasma (ICP) RIE process. This process is adapted from [28] using ZEP rather than HSQ resist.

The critical temperature T_c of this device was approximately 6.5 K, defined as the point at which device resistance drops to zero [see Fig. 1(c)]. The device T_c is higher than the thin-

#260601 Received 7 Mar 2016; revised 13 May 2016; accepted 18 May 2016; published 14 Jun 2016

film T_c of MoGe [13] and MoSi [14] reported previously, indicating that the superconducting gap energy of this device is large enough to allow the device to operate at $\sim$ 2.5 K which is achievable in a simpler two-stage closed-cycle cryocooler [9]. The device T_c is also lower than typical NbN/NbTiN thin-film T_c [13], thus the device should have high intrinsic detection efficiency for long wavelength photons.

Light absorption efficiency is determined by two factors, the strength of the evanescent field overlap with the nanowires and the field-nanowire interaction length. The absorption efficiency of MoSi hairpin SNSPD at 1550 nm wavelength as a function of hairpin length and nanowire width was numerically simulated by using a finite difference time domain (FDTD) solver (Lumerical). The refractive index and extinction coefficient of MoSi film at 1550 nm are $n = 5.2502$ and $k = 4.7736$, respectively, which were measured by variable-angle spectroscopic ellipsometry (VASE). As shown in Fig. 1(d), for 140 nm wide MoSi nanowires, in theory more than 95% absorption efficiency is obtained for hairpin length longer than 5 μm.

The nano-optical characterization of the MoSi SNSPD reported in this paper was performed at 350 mK. Such low temperature was achieved with a three-stage helium sorption refrigerator [29] from Chase Research Cryogenics, as shown in Fig. 2(a). It was attached to a stand-off stage thermally linked (via flexible oxygen-free copper braids which also provide vibration damping [30]) to the 3 K stage of a Cryomech PT405 pulse tube cold head with low vibration remote motor option.

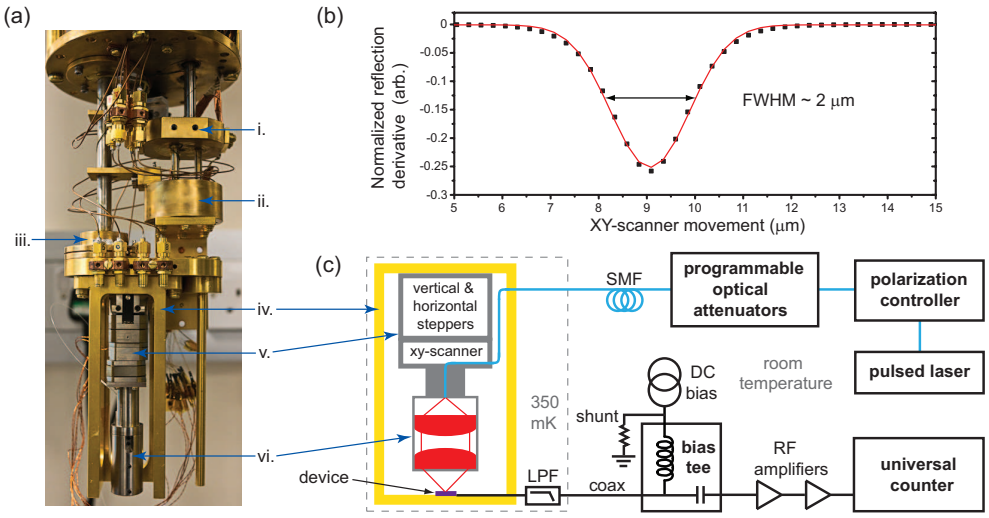

Fig. 2. (a) Photograph of three-stage helium sorption refrigerator and nano-optical setup: i. film burning stage, ii. ^{4}He buffer stage, iii. ^{3}He cold head, iv. nano-optical housing, v. piezoelectric positioners, and vi. confocal microscope. (b) Gaussian fit (red solid line) of the differentiated Au contact pad edge profile at λ = 1550 nm (black dotted line). (c) Nano-optical configuration for single photon measurements, as well as room temperature optics and electronics for counts map and detection efficiency measurements. Piezoelectric positioners and confocal microscope are mounted in a gold plated oxygen-free copper housing, which is attached to ^{3}He cold head. SMF: single-mode fiber; LPF: low pass filter.

Optical fiber feedthrough with single-mode fibers (Thorlabs 1310BHP) and a fiber-based confocal microscope [31] were adopted for device illumination, as shown in Figs. 2(a) and 2(b). The confocal microscope consisted of two aspheric lenses and a titanium lens tube, which was attached to the bottom of a stack of four piezoelectric positioners (Attocube Systems). A vertical piezoelectric stepper was used for confocal microscope focusing, two horizontal

#260601 Received 7 Mar 2016; revised 13 May 2016; accepted 18 May 2016; published 14 Jun 2016

piezoelectric steppers were used for large area (5×5 mm^2) scanning (locating the device region on chip), and a piezoelectric xy-scanner was for small area ($\sim 30 \times 30$ μm^2) high resolution device surface scanning. All positioners were controlled by an Attocube ANC350/SCAN multi-functional piezo motion controller. The steppers' positions were read out via resistive sensors; the scanner's positions were calibrated by using an in-house fabricated Au checkerboard chip. The spot size of light focused on the surface of SNSPD chip was determined by measuring the SNSPD Au contact pad edge profile. As plotted in Fig. 2(b), the full width at half maximum (FWHM) diameter of focused light spot was approximately 2 μm with a Gaussian profile.

To minimize the heat load to the ^{3}He cold head of the sorption refrigerator, and in tandem to maintain low electrical resistance on the measurement lines, center pin silver plated beryllium copper semi-rigid coaxial cables were used from room temperature to base temperature for SNSPD bias and readout. In the same manner, niobium-titanium superconducting woven looms were used for the piezoelectric positioner wiring from pulse tube 3 K stage to ^{3}He cold head.

3. Results and disscussion

To characterize the MoSi SNSPD, we first used the nano-optical setup as a scanning optical microscope to map the surface of the chip and to locate the device. A 1550 nm wavelength Thorlabs fiber-coupled benchtop superluminescent diode (S5FC1550P-A2) source (2.5 mW, FWHM linewidth = 90 nm) was used to illuminate the chip. As the horizontal piezoelectric positioners moved, light reflected from chip surface was collected by the confocal microscope and directed to a InGaAs detector (Thorlabs DET10C/M) via a circulator at room temperature. Figure 3(a) shows normalized output voltages of the InGaAs detector as a function of position over the device region. Although the xy-scanner's positioning resolution is below 100 nm, the resolution of this reflection map is limited by the spot size of focused laser beam [see Fig. 2(b)], which is much larger than the width of the SOI waveguide (between the green dashed lines) where the MoSi hairpin (illustrated by the red solid hairpin) is located.

We then measured the dark count rate (DCR) of the MoSi device without illumination, by current biasing the SNSPD via a bias tee (Picosecond Pulse Labs 5575A), amplifying dark count pulses with two room temperature radio-frequency (RF) amplifiers (RF Bay LNA-580 and LNA-1000, passband 10 to 580 MHz, total gain 56 dB), and registering the pulses by an Agilent 53131A universal counter [see Fig. 2(c)]. A Mini-Circuits VLFX-540 high rejection low pass filter (LPF) of passband from DC to 540 MHz was mounted close to the sample at 350 mK, to filter out high-frequency electrical and thermal noise on the measurement line. To prevent the SNSPD from latching into a finite voltage state [32], an 18 Ω shunt resistance was used at room temperature [see Fig. 2(c)]. The bias current dependent DCR is shown in the top panel of Fig. 3(c). A plateau of DCR $<$ 10 Hz can be found at bias current I_b below 38.1 μA which is approximately 93% of the measured critical current $I_c = 41$ μA. Low DCR region of this device is wider than other MoSi SNSPDs' reported in [16] (0.9 I_c) and [14] (0.8 I_c), mainly due to the lower operating temperature and effective filtering of the measurement line in our case. Unlike the nearly linear dependence of $\log(\mathrm{DCR}) \propto I_b$ for MoSi meander devices reported in [15], for our hairpin device the DCR exhibited a sharp jump (from 10 Hz to $> 10^4$ Hz) when I_b was slightly larger than 38.1 μA. The DCR rose steeply to saturate the universal counter at 38.4 μA. The abrupt increase of DCR is due to the very low operating temperature (350 mK) in our measurements. Similar behavior of DCR was observed in the fiber-coupled WSi SNSPD at temperatures below 1.4 K, as shown in Fig. 3(b) of [12], and is attributed to the sensitivity of the low energy gap superconductor SNSPD to mid infrared photons when biased.

The photoresponse uniformity of the SNSPD was confirmed by mapping the device area with a pulsed 1550 nm laser at a repetition rate of 1 MHz. The input photon flux into the microscope was maintained on average below 1 photon per pulse. The same device area as reflection map

#260601 Received 7 Mar 2016; revised 13 May 2016; accepted 18 May 2016; published 14 Jun 2016

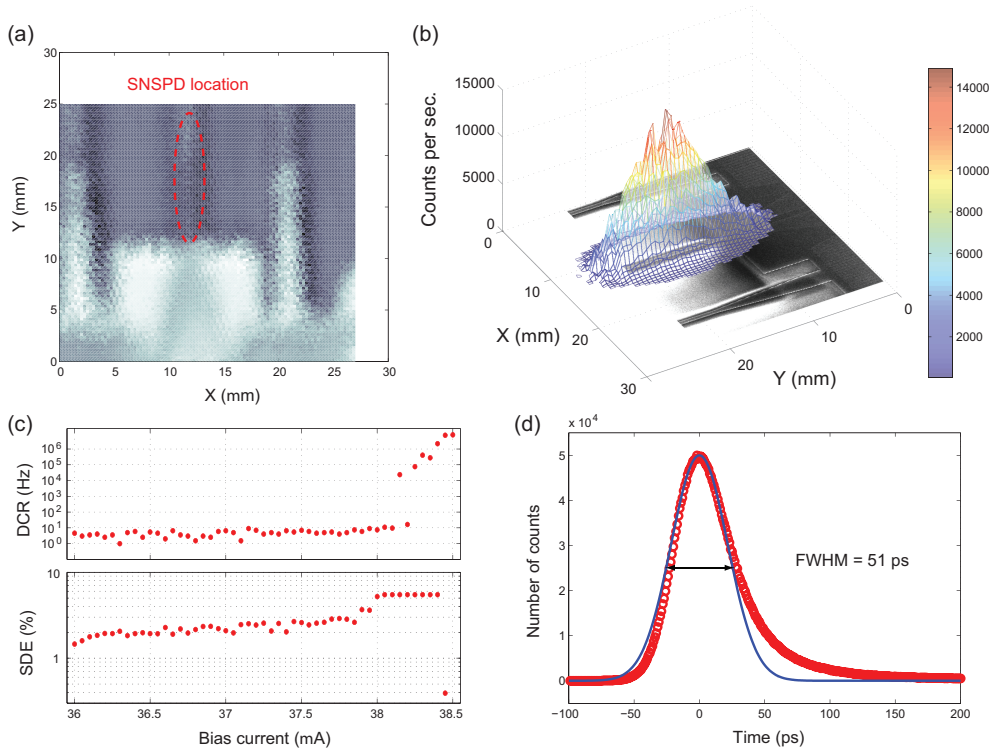

Fig. 3. (a) Reflection map of the device region. (b) Counts map of the device region with $I_b = 37\ \mu$A. The grayscale image on the base of the figure is a SEM photo of the device region. (c) Top: the DCR versus bias current. Bottom: the SDE versus bias current. (d) TCSPC instrument response histogram (red circles) with a Gaussian fit (blue solid line) at $I_b = 38\ \mu$A. The FWHM timing jitter is 51 ps.

[Fig. 3(a)] was scanned. The registered photon counting events are shown as the (color gradient) three-dimensional surface map in Fig. 3(b), and a SEM image of the same area is placed under the surface map. The FWHMs of this counts map are approximately 2.5 μm in the X-direction and 10.5 μm in the Y-direction, which match the spot size and the hairpin length, respectively. The uniform photoresponse over the device indicates that there is no defect or constriction in the MoSi nanowire.

The bottom panel of Fig. 3(c) shows measurements of the SDE at 1550 nm wavelength versus bias current, carried out at where the maximum photon counting rate was found in Fig. 3(b). The optical power is determined at the fiber input of the cryostat; the measured SDE includes the optical losses in the delivery fiber, microscope, and geometrical loss as the optical spot illuminates significantly larger area than the SNSPD hairpin. The SDE is $> 1\%$ over a wide bias range and reaches a maximum of $\sim 5\%$ when $I_b \geq 38\ \mu$A. There is a small optimal bias window, $38\ \mu\text{A} \leq I_b \leq 38.1\ \mu$A, in which the SDE is maximized and the DCR is only about 10 Hz. As noted earlier, our 2 μm FWHM Gaussian optical spot is much larger than the hairpin width, and thus the geometrical optical coupling efficiency is at most 13%. Moreover considering the measured optical properties of MoSi, and the vertical optical structure, matrix transfer method simulations indicate an absorption of 47% under perpendicular illumination. Therefore 5% SDE [Fig. 3(c)] and uniform photoresponse map [Fig. 3(b)] indicate that we have high absorption and triggering along the length of the hairpin. It is therefore reasonable to infer that moving

#260601 Received 7 Mar 2016; revised 13 May 2016; accepted 18 May 2016; published 14 Jun 2016

to optical coupling via the waveguide, we would achieve high efficiency [as predicted by the simulation of Fig. 1(d)] for this device.

A 1550 nm femtosecond fiber laser and a time-correlated single-photon counting (TCSPC) module (PicoQuant HydraHarp 400) were used for timing jitter measurements [illustrated in Fig. 3(d)]. We acquired the instrument response histograms without and with the LPF at 350 mK [see Fig. 2(c)]. The FWHM timing jitters were extracted from Gaussian fits of these histograms. Without the LPF, the jitter is 57 ps FWHM. By using the LPF to filter out high-frequency noise, the jitter is improved to 51 ps FWHM, as shown in Fig. 3(d). The histogram shown in Fig. 3(d) is asymmetric comparing with the Gaussian fit. Similar asymmetries have been observed in other SNSPDs based on NbTiN [24, 33].

4. Conclusion

In conclusion, we have carried out detailed low temperature nano-optical studies of SOI waveguide integrated MoSi SNSPDs, which demonstrates that these devices are a promising candidate for on-chip single photon detection in optical quantum information processing. We have developed an easy-to-maintain closed-cycle ^{3}He cryogenic system for nano-optical characterzation at 350 mK. We have measured the refractive index n and extinction coefficient k of $Mo_{83}Si_{17}$ film by VASE, and from the numerical simulations we have shown that MoSi hairpin has very high light absorption rate via the waveguide underneath. In this study we have used perpendicular illumination to study MoSi hairpin device uniformity. The high uniformity has been confirmed by photoresponse mapping. The maximum system efficiency achieved (5%) in this device, inclusive of optical coupling losses and expected absorption, implies that moving to optical coupling via the waveguide in future devices, we expect to achieve near unity efficiency. It is necessary to meet these demanding single-photon detector specifications for scalable on-chip quantum information processing [34]. This is the first batch of MoSi hairpin devices we have fabricated and tested. We have since fabricated a number of such devices with good uniformity and yield. On-chip grating couplers have also been fabricated on subsequent batch. Our next step is a full characterization of MoSi hairpin SNSPD with optical coupling via the waveguide. The high T_c (6.5 K) and large I_c (41 μA at 350 mK, 32 μA at 2.5 K) suggests these MoSi devices could be operated with good performance at $\sim$ 2.5 K which is easily achievable in closed-cycle Gifford-McMahon refrigerators.

Acknowledgment

The authors thank Dr. Michael Tanner and Prof. Richard Warburton for assistance with the cryostat and nano-optical design, the University of Glasgow School of Engineering mechanical workshop for precision machining of bespoke parts, Dr. Stephen Thoms of the University of Glasgow James Watt Nanofabrication Centre for expert support on multi-step electron beam lithography process development, and Dr. Alessandro Casaburi for useful discussions. R. H. H. acknowledges support via the Engineering and Physical Sciences Research Council (EPSRC) grants EP/I036273/1, EP/J007544/1 and EP/L024020/1, and a European Research Council Consolidator Grant. Z. H. B. acknowledges support through EPSRC grant EP/I036303/1.

#260601 Received 7 Mar 2016; revised 13 May 2016; accepted 18 May 2016; published 14 Jun 2016